Chemical Geology 528 (2019) 119283

Contents lists available at ScienceDirect

Chemical Geology

journal homepage: www.elsevier.com/locate/chemgeo

Micron-scale distribution of metals in Cambrian metalliferous shales, South China: Insights into local biologically driven redox disequilibrium

Anaïs Pagès[a,*], Steve Barnes[a], Susanne Schmid[a], Chris Ryan[b], David Paterson[c], Colin MacRae[b], Jamie Laird[b], Margaux Le Vaillant[a], Haifeng Fan[d,e], Hanjie Wen[d,e]

[a] CSIRO Mineral Resources, Kensington, WA 6151, Australia
[b] CSIRO Mineral Resources, Clayton, VIC 3168, Australia
[c] Australian Synchrotron, ANSTO, Clayton, VIC 3168, Australia
[d] State Key Laboratory of Ore Deposit Geochemistry, Institute of Geochemistry, Chinese Academy of Sciences, Guiyang 550002, Guizhou, China
[e] University of Chinese Academy of Sciences, Beijing 100049, China

ARTICLE INFO

Editor: Hailiang Dong

Keywords:
Metalliferous black shales
Synchrotron
XANES
PIXE
Redox states
Organic matter

ABSTRACT

Early Cambrian black shales of the Niutitang Formation are found across the Yangtze Platform in a 1600-km belt extending across south China. A thin organic matter-rich layer in the lowermost part of this formation contains exceptional concentrations in Mo, Ni, Se, Re, Os, As, Hg, Sb, Ag, Au, Pt, Pd, and Ag. Due to their extreme metal enrichment, these black shales provide a rare opportunity to study the interface between semi-metals, metals and biogenic material. We report the first detailed μm-scale investigation of metal distributions and associations in samples from two sites, Zunyi and Sancha, located hundreds of km apart, using a combination of analytical techniques including X-ray fluorescence (XRF) mapping, scanning electron microscopy (SEM), Synchrotron-based XRF mapping, electron probe micro-analyser (EPMA), particle induced x-ray emission (PIXE) probe and x-ray absorption near-edge structures (XANES) imaging. Strong μm-scale variations in metal and semi-metal distributions were highlighted by Synchrotron-based XRF mapping of samples from both sites. At both locations, U is present within phosphorite nodules. Arsenic, Mo and Se are particularly abundant in the organic-rich matrix, showing strong associations with organic matter. Nickel, however, shows different distributions between the two sites. It is mainly present in association with the organic matter at the Sancha site while it is found in abundance in millerite at the Zunyi site, suggesting slightly different local conditions at Zunyi favouring Ni-S associations over Ni-organic matter. At both sites, biogenic structures were re-mineralised with laminations dominated by different metals, indicating a likely control of organic matter over metal distributions. In addition, the XANES imaging highlighted different redox states of As over μm-scale areas. While As^{-1} appears to be mainly present in pyrite, As^{+3} was mainly detected in association within the carbon and MoS_2 mixed layer phase (MoSC). Overall, the present results emphasize the complexity of metal associations in this mineralised layer, the significant role of organic matter in the accumulation and precipitation of metals and semi-metals in these metalliferous shales and highlight how biogenic activity can induce μm-scale variations in redox conditions in sediments.

1. Introduction

Early Cambrian black shales of the Niutitang Formation were deposited throughout the Yangtze Platform, covering a belt extending up to 1600 km across south China. In the lowermost part of this formation, a thin layer containing exceptional enrichment of metals and semi-metals is present, associated with abundant organic matter. Molybdenum, Ni, Se, Re, Os, As, Hg and Sb are over 1000 times enriched in comparison to bulk continental crust, and Ag-Au-Pt-Pd are > 100 times enriched compared to the continental crust (e.g. Fan, 1983; Coveney and Chen, 1991; Lott et al., 1999; Mao et al., 2002). Despite the fact that mineralised horizons have been reported at different sites detected hundreds of km apart, it remains unclear whether this ore body forms a continuous layer across South China. In addition, the origin of these deposits remains highly controversial. Two main concepts have been proposed. The first one involves direct metal scavenging from seawater (e.g. Mao et al., 2002; Lehmann et al., 2007; Xu et al., 2013; Lehmann et al., 2016; Lehmann et al., 2007; Pagès

* Corresponding author.
E-mail address: Anais.pages@csiro.au (A. Pagès).

https://doi.org/10.1016/j.chemgeo.2019.119283
Received 29 May 2019; Received in revised form 15 August 2019; Accepted 17 August 2019
Available online 19 August 2019

et al., 2018). The second one suggests a contribution from hydrothermal seafloor venting (Coveney and Nansheng, 1991; Lott et al., 1999; Steiner et al., 2001; Jiang et al., 2006). Pašava et al. (2008), however, proposed mixed metal sources with specific elements such as Mo and P deriving from seawater and others (e.g. Ag, Cu, Ni, Pb, PGE, Zn, V) from hydrothermal venting, while Emsbo et al. (2005) suggested that the extreme metal enrichment observed in these shales would be related to the presence of strong bioproductivity and the occurrence of anoxic to dysoxic conditions. According to Emsbo et al. (2005), the discharge of multiple hydrothermal fluids including H_2S-rich brines, petroleum and oxidized brines, providing large quantities of biolimiting nutrients such as NH_4, trace metals Si and Ba into the basin, would have further promoted bioproductivity.

Due to their extreme enrichment in an array of metals, these Cambrian black shales provide a fantastic opportunity to study metal and semi-metal distributions and associations at µm-scale in an organic matter-rich matrix. The main goals of the present study include the comparison of metal distributions in samples of the mineralised horizon from Zunyi and Sancha in order to compare mineralisation style in two sites located 600 km apart in South China. The present study reports for the first time a detailed µm-scale investigation of metal distributions and associations in samples from both the Zunyi and Sancha sites, using a combination of analytical techniques including X-ray fluorescence (XRF) mapping, scanning electron microscopy (SEM), synchrotron-based XRF mapping, electron probe micro-analysis (EPMA), particle induced x-ray emission (PIXE) probe and x-ray absorption near-edge structures (XANES) imaging. This study offers greater understanding of metal associations at µm-scale in this highly complex mineralised horizon and provides further insight into the role of redox conditions in the genesis of the mineralisation

2. Geological setting

2.1. Metalliferous black-shales of South China

The Yangtze Platform of South China contains widely exposed Neoproterozoic and Early Cambrian sedimentary units. The depositional facies represent a shelf environment with cycles of transgressions and regressions (Steiner et al., 2001). The Neoproterozoic-Cambrian sedimentary facies shows a clear transition from a shallow shelf environment with deposition of carbonates and phosphorites in the NE towards a protected and deep basinal facies containing black shales and cherts in the SE (Zhu et al., 2003; Wallis, 2007).

Neoproterozoic Formations include the Nantuo, Doushantuo, and Dengying Formations. The Nantuo Formation contains glaciogenic rock deposited 630 Ma during the Neoproterozoic Marinoan ice age (Gradstein et al., 2004). The Doushantuo Formation, deposited between 635 and 551 Ma (Condon et al., 2005), includes carbonaceous mudstone and dolomite with interbedded phosphorite. The Niutitang Formation unconformably overlies the Dengying Formation. The Niutitang Formation mostly contains black shales but phosphorite and barite units have also been reported. A polymetallic layer, with a thickness of 3 to 5 cm, is present locally in the lowermost part of the Formation. This ore layer occurs sporadically over a 1600 km length along the margins of the Yangtze Platform, covering six provinces in SE China (Fig. 1). The ore layer is commonly a few centimetres thick, although it extends up to 2 m at the Huangjiawan mine in Zunyi (Zeng, 1998). This mineralised layer is extremely enriched in Mo, Ni, Se, Re, Os, As, Au, Hg, Sb, Ag, Pt, and Pd, on the order of 10^6 to 10^9 in comparison with seawater concentrations (Murowchick et al., 1994; Li and Gao, 2000; Mao et al., 2002). The high thermal maturity of the bulk organic matter corresponds to semi-anthracite to anthracite coalification stage (Kříbek et al., 2007). It was suggested that the organic matter could have derived from in-situ products of planktonic and benthic organisms (Orberger et al., 2007). The Niutitang Formation is overlain by shales and siltstones of the Mingxinsi Formation, sandy shales of the Jindingshan Formation and dolomites of the Qingxudong Formation.

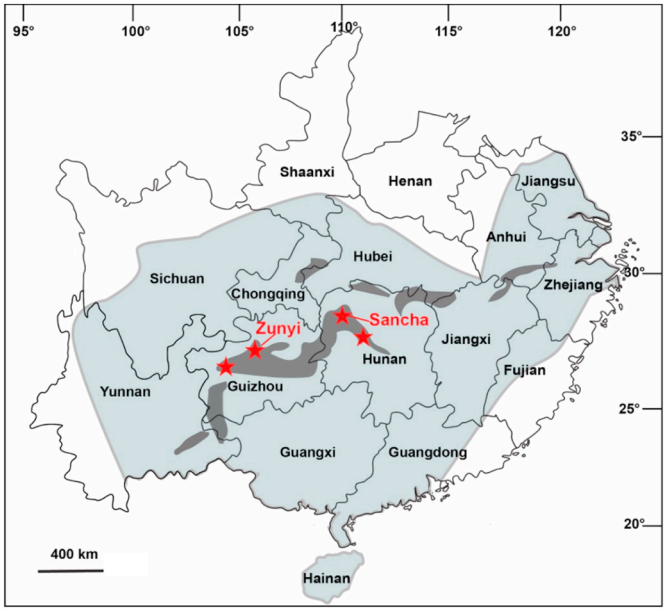

Fig. 1. Map of the Yangtze platform, South China. The light grey area represents the Yangtze platform and the dark grey areas indicate black shale distributions in the platform. The red stars indicate locations where the mineralised horizon has been reported, including the Sancha and the Zunyi sites. (For interpretation of the references to colour in this figure legend, the reader is referred to the web version of this article.)

3. Material and Methods

3.1. Sampling

Twenty-nine outcrop samples were collected from two sites in China. The two sites, referred to as Zunyi and Sancha (Fig. 1), are located 600 km apart and both show the presence of a mineralised layer.

The Ni–Mo–PGE ore layer of Dazhuliushui (referred to as the Zunyi site in the present study) is located about 26 km east of Zunyi city, Guizhou Province (Fig. 1). Neoproterozoic units of the Nantuo, Doushantuo and Dengying Formations, and black shale of the Cambrian Niutitang Formation are exposed. The Ni–Mo–PGE sulfide ore layer is located between 4 and 8 m above the contact with the Dengying Formation.

The Sancha Ni–Mo–PGE ore layer in Hunan Province is located about 380 km northeast of the Dazhuliushui mine site (Fig. 1). At this site, the Niutitang Formation unconformably rests on the Dengying Formation. The lowermost part of the section includes bedded and nodular phosphate. The sulfide ore layer is about 1 m above the unconformity with the dolomite of the Dengying Formation.

3.2. Scanning electron microscopy (SEM)

Thin sections (30 µm thick) of the mineralised layer were prepared and studied by SEM at the Australian Resources Research Centre. Backscattered electron images were obtained with a Zeiss Ultra-Plus FEG-SEM coupled with a Bruker X-Flash energy dispersive X-ray spectroscopy (EDS) detector for elemental analyses. An accelerating voltage of 20 kV in high current mode was used.

3.3. Desktop-based XRF microscopy

Thin-sections were analysed by XRF mapping at the Australian Resources Research Centre were obtained using a Bruker M4

TORNADO™ equipped with a rhodium target X-ray tube operating at 50 kV and 500 nA and an XFlash® silicon drift X-ray detector. Collected data were processed using the Bruker ESPRIT software. Maps were created using a 35-μm spot size on a 25-μm raster with dwell times of 5 ms per pixel. Maps are represented as unquantified background corrected peak height data for Kα peaks for each element.

3.4. Synchrotron-based XRF microscopy

Thin-sections were also analysed by synchrotron-based X-Ray Fluorescence Microscopy (XFM). The Maia detector array on the XFM beamline, at the Australian Synchrotron in Melbourne, allows the production of elemental maps with approximately 10 ppm detection limits and a resolution of up to 2 μm at short dwell time per pixel (Ryan et al., 2010). Detailed maps were produced over areas of about 3 cm^2 using a beam energy of 18.5 keV, a spot size of 2 μm and dwell times per pixel of 0.97 ms. These elemental maps represent an effective way of precisely mapping element association on the scale of a few cm^2 in a matter of a few hours. The high-definition images obtained with the Maia detector allow the detection of metal segregation on a wide range of spatial scales. Standard foils of Fe, Mn, Pt and YF_3 were analysed daily to monitor energy drift and allow calibration of the ion chamber used to measure X-ray flux. GeoPIXE™ software was used for post collection data processing. Spectra were fitted using yield files which are calculated based on the given mineral assemblages and compositions of the samples that were being mapped. Quantified element concentrations were generated from the spectra using the Dynamic Analysis methods (Ryan et al., 2010).

3.5. XANES imaging

Synchrotron-based XRF maps, obtained at the Australian Synchrotron, were collected at eighty one irregularly spaced monochromator energies that spanned the As-K edge, averaging 1 eV per step, with 0.5 eV steps across the edge. The As concentrations at each pixel in the SXRF map, at each monochromator energy, were extracted and used to construct XANES spectra at each pixel (Etschmann et al., 2014). An overview map of each sample was performed covering areas of about 8 × 4 mm^2 at 2 μm pixels with a transit time of 1.18 ms per pixel. Regions of interest were selected from these overview scans for detailed XANES mapping. These XANES stacks maps (typically 1.28 × 0.4 mm) at 2 μm pixel and 1.0 ms transit per pixel, repeated over a sequence of 81 energies spanning the K absorption edge of As.

3.6. PIXE probe

As Mo cannot be efficiently mapped using XFM at the chosen beam energy as the K lines are not excited and the L lines compete with S, Mo distribution was obtained by PIXE mapping. PIXE microscopy using a 3 MeV proton beam was performed on the CSIRO Nuclear Microprobe (NMP) (Ryan, 2004) to map major, minor and trace element concentrations. Protons were focused to an approximate 2 μm spot prior to analysis and a HP Ge x-ray detector mounted at a back angle of 45 degrees was used to collect x-ray spectra. A 150 μm Al filter placed over the detector face attenuated contributions from lighter elements in the matrix, thereby reducing instrument saturation affording larger beam currents and improved statistics for minor and trace elements. The DAQ-36 data collection system (Laird et al., 2017) was used to record data in list-mode as the beam was scanned in 2 μm steps with pixel dose normally being ~50 pC to ensure ppm level sensitivity for a broad range of elements. The GeoPIXE package incorporating Dynamic Analysis (DA) was used for offline PIXE analyses (Ryan and Jamieson, 1993) assuming a pyrite host matrix.

3.7. EPMA

EPMA mapping was performed on the CSIRO JEOL8500F EPMA equipped with four wavelength dispersive spectrometers (WDS), two Bruker XFlash 6|10 energy dispersive spectrometers (EDS) and an integrated optical spectrometer to spectrally detect the cathodoluminescence signal.at 15 kV, 50 nA, and a 30 ms dwell. The step size was 1 μm and the beam was defocused to match the step size. The samples were coated with 10 nm of carbon prior to mapping using a carbon arc coater. Fe, Kα; S, Kα; and C, Kα; were mapped using WDS, along with hyperspectral x-ray data collected using energy dispersive spectrometers (EDS). Elements that were not measured by WDS were extracted from the hyperspectral EDS data. Measuring both ED and WD signals simultaneously ensured that the complete chemical spectrum, at each step interval in the map, was obtained. After mapping, the element distribution data were manipulated using the software package CHIMAGE (Harrowfield et al., 1993). CHIMAGE allows the individual element data to be displayed as either single element distribution scatter plots or as combined element maps (where data for two or more elements are combined on each mapped region).

4. Results

4.1. XRF mapping (desktop instrument)

Microbeam desktop XRF mapping was conducted on samples from the Zunyi and Sancha sites (Fig. 2). Phosphorite nodules and fragments were consistently detected in high abundance at both sites in the mineralised layer and present different sizes and shapes. In Fig. 2A and B, the mineralised layer from Sancha displays a zone with abundant phosphorite nodules and fragments. As is accumulated on the edge of the phosphorite nodule and is also present in the matrix. Ni is strongly accumulated in the lower part of the sample, and is sparsely present in association with lenses of phosphorite. The lower part of this sample shows laminations of sulfides. The second sample from the mineralised layer in Sancha (Fig. 2C and D) contains a ~25 mm diameter phosphorite nodule in the left part of the map and an enrichment in As-rich sulfides and V in the right part of the map.

The first sample from the mineralised layer in Zunyi (Fig. 2E and F) is mostly dominated by fragmented parallel laminations of sulfides, although the upper section of the sample contains a phosphorite nodule (~ 4 mm across) and few phosphorite fragments. The uppermost zone of the sample is rich in V. The second sample from the mineralised layer in Zunyi (Fig. 2G and H) highlights a highly brecciated texture with abundant phosphorite nodules and fragments. Nickel and As sulfides are also present as small lenses while V is most abundant in the lowermost section of the sample and is dispersed in the uppermost part of the sample that mostly contains the fine matrix.

4.2. Synchrotron-based XFM and PIXE mapping

4.2.1. Investigation of phosphorite nodules

Since P is too light to be detected on the XFM beamline, Ca was used as a proxy to characterise the phosphorite nodules. At both locations, Sr seems fairly abundant in the phosphorite nodules (Fig. 3B and E). Nickel is present in restricted areas within the nodules, as highlighted in Fig. 3A and D while As seems to be locally coating the phosphorite nodules. Uranium is dispersed in the phosphorite from Sancha while it is present in a single zone within the phosphorite from Zunyi (Fig. 3C and F respectively). Iron is not found within the nodules but instead is present as pyrite in the vicinity of the nodules (Fig. 3B and D).

4.2.2. Metals and semi-metals associations

Nickel, As, Cu, Zn and Fe distributions were mapped by Synchrotron-based XFM. In the samples from Sancha, Ni and As distributions are quite complex, with abundant μm-scale variations

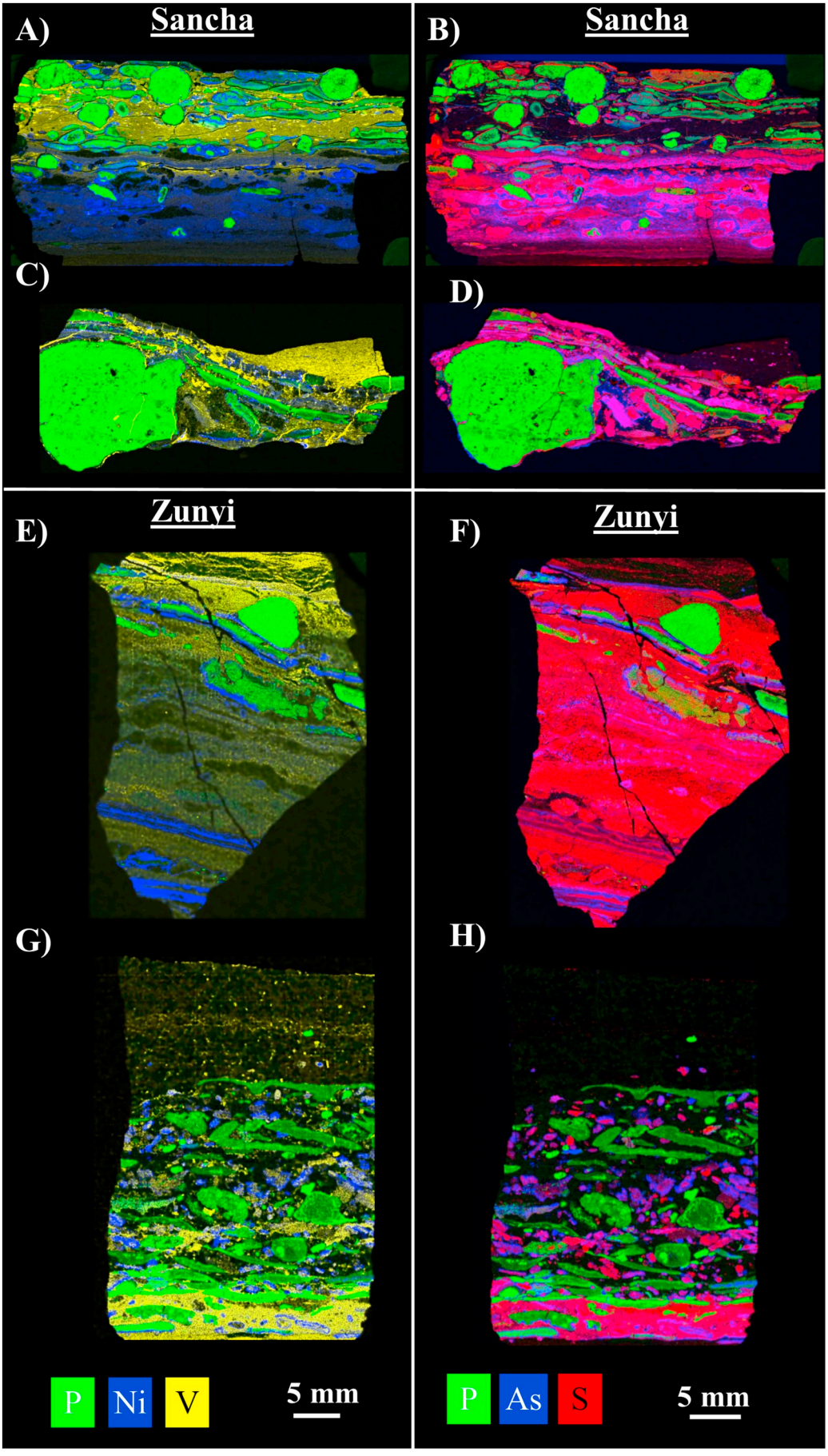

(caption on next page)

Fig. 2. Microbeam XRF elemental mapping of P (in green), Ni (in blue) and V (in yellow) (maps A, C, E and G) and P (in green), As (in blue) and S (in red) (maps B, D, F and H) in samples from the Sancha mineralised layer (maps A-D) and from the Zunyi mineralised layer (maps E-H). (For interpretation of the references to colour in this figure legend, the reader is referred to the web version of this article.)

(Fig. 4). Pyrite aggregates are found throughout, as highlighted by Fe distributions, but are not consistently observed in close vicinity to As or Ni-rich phases. A minority of pyrite aggregates contain detectable Ni and As. Zinc is present as hot spots, near As and Ni-rich phases while Cu hot spots are sparse and found in close vicinity to As-rich phases. Selenium is most abundant in between the pyrite aggregates and the Ni and As-rich phases. Nickel and Se present overlaps in their distributions in specific locations (Fig. 4C).

In addition, also in the samples from Sancha, PIXE mapping revealed that Mo is associated with As or Fe in few localised areas, however, Mo shows no distribution overlap at all with Ni (Fig. 5). Abundant pyrite aggregates, as highlighted by the distribution of Fe, are present in close vicinity to the Mo-rich phases. In samples from Zunyi, As-rich and Ni-rich layering is observed (Fig. 4D). Similar to samples from Sancha, pyrite aggregates are also observed but do not display any association with Ni or As. Zinc is observed as hot spots, often associated with Ni. Copper seems to be localised and is observed in association with Ni and As-rich phases. Similar to samples from Sancha, in samples from Zunyi, Se is abundant and is detected in between pyrite aggregates and As-rich phases.

4.2.3. Mineralised biogenic features

Samples from Zunyi and Sancha both present biogenic morphological features that have been re-mineralised with various metals. For instance, Fig. 6A (Sancha mineralised layer) highlights an elongated shape made of Ca with abundant As located on the edge. Fig. 6B (Sancha mineralised layer) shows a rounded and elongated structure (> 1 mm long) that contains a complex and intricate internal configuration, strongly suggesting a biological origin. Abundant Ni is found within and on the edges of this biogenic feature, along with disseminated As and Fe present in arsenopyrite. Next to this biogenic feature, abundant framboidal pyrite was detected, as highlighted by disseminated Fe. The sample from Zunyi (Fig. 6C) also contains biogenic features showing resemblances (e.g. shape and size range) to the ones observed in the sample from Sancha. However, the biogenic structures presented in Fig. 6C clearly display the presence of fine laminations demonstrating alternating enrichment in Ni, As and Fe. These biologically-derived structures are also surrounded by finely disseminated framboidal pyrite, as highlighted by the Fe distribution.

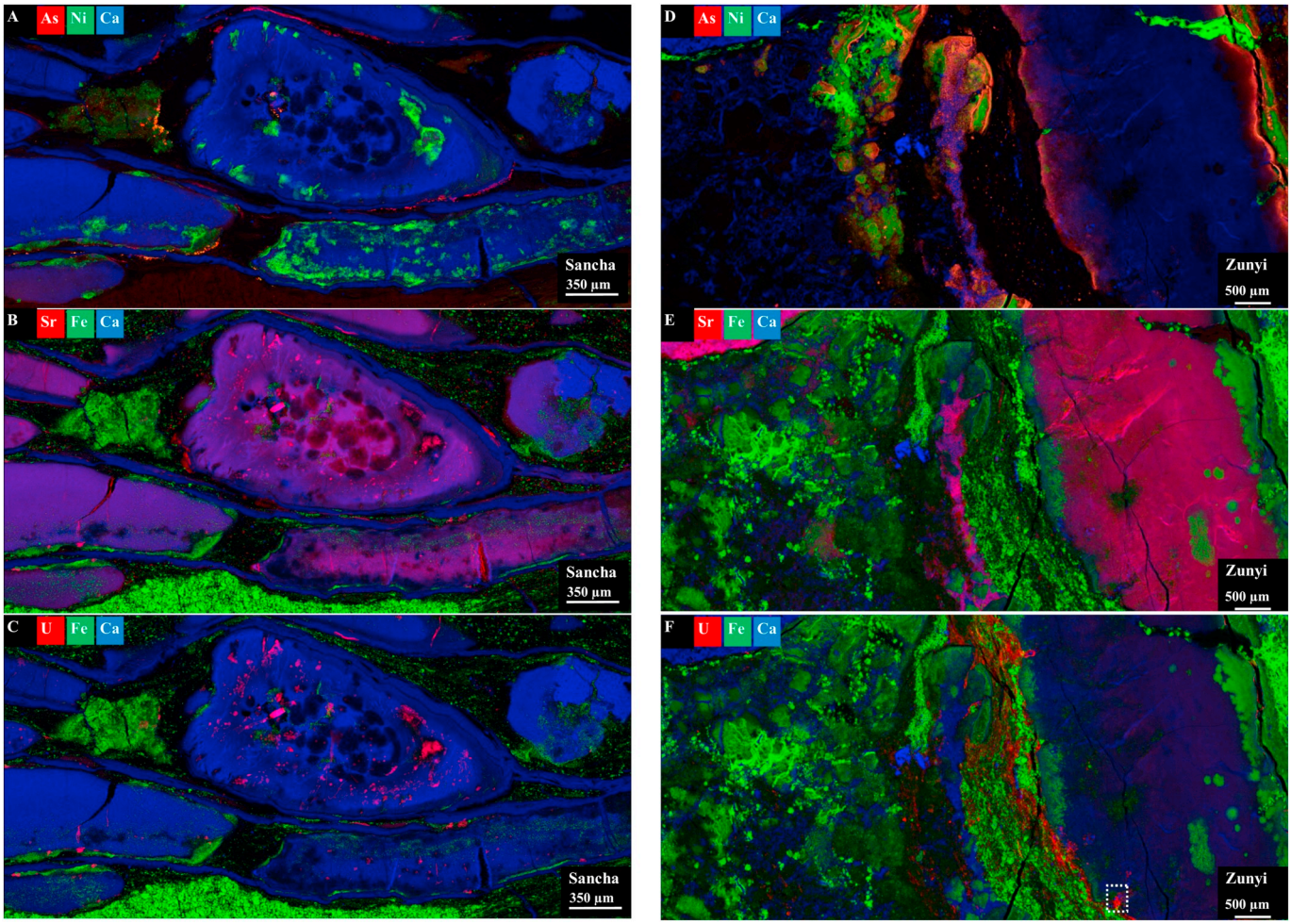

Fig. 3. Synchrotron-based XFM element maps of phosphorite of samples from the Sancha mineralised layer (A, B, C) and the Zunyi mineralised layer (D, E, F). A and D) As (in red), Ni (in green) and Ca (in blue) distributions. B and E) Sr (in red), Fe (in green) and Ca (in blue) distributions. C and F) U (in red), Fe (in green) and Ca (in blue) distributions. The white rectangle in F) highlights the area where U is detected within the phosphorite. (For interpretation of the references to colour in this figure legend, the reader is referred to the web version of this article.)

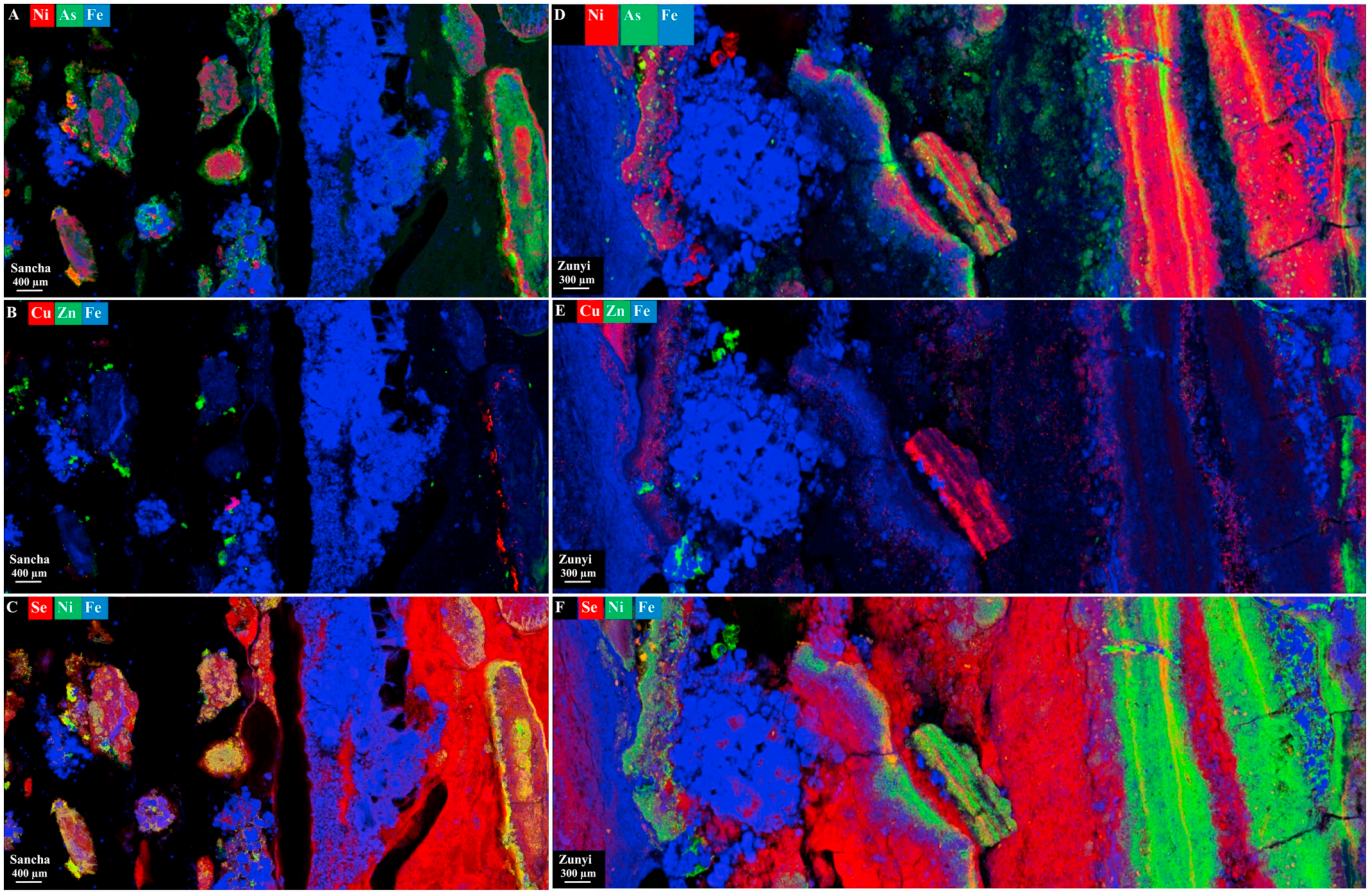

Fig. 4. Synchrotron-based XFM element maps of samples from the Sancha mineralised layer (A, B, C) and the Zunyi mineralised layer (D, E, F). A and D) Ni (in red), As (in green) and Fe (in blue) distributions, B and E) Cu (in red), Zn (in green) and Fe (in blue) distributions and C and F) Se (in red), Ni (in green) and Fe (in blue). (For interpretation of the references to colour in this figure legend, the reader is referred to the web version of this article.)

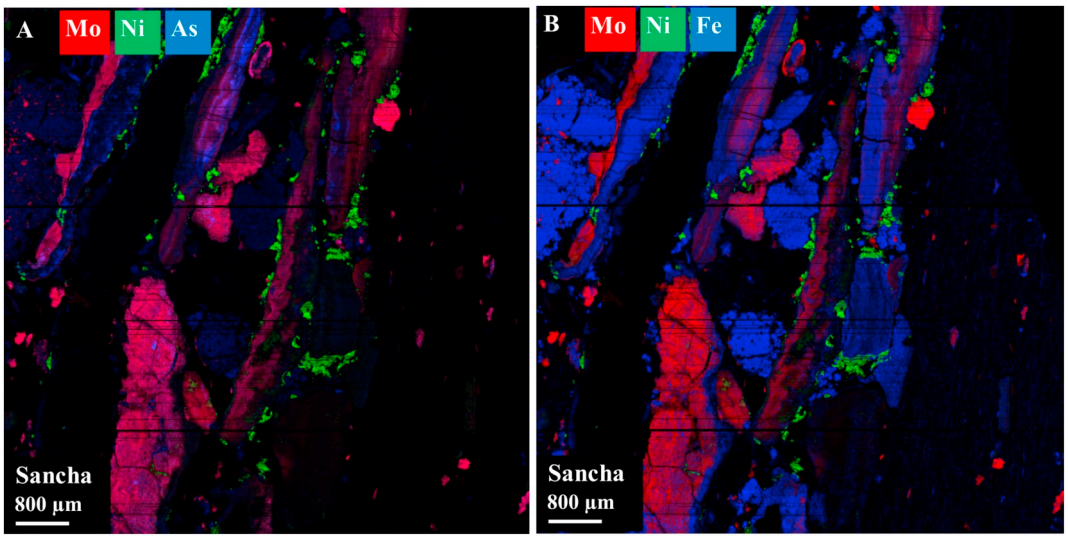

Fig. 5. PIXE element maps of a sample from the Sancha mineralised layer highlighting Mo distributions (in red) with A) Ni (in green) and As (in blue) distributions and B) Ni (in green) and Fe (in blue) distributions. (For interpretation of the references to colour in this figure legend, the reader is referred to the web version of this article.)

4.3. Redox states of As

A specific area containing arsenopyrite and organic matter-rich matrix was selected in a sample from the Sancha mineralised layer in order to investigate different redox states of As by XANES imaging. Two redox states of As (As^{-1} and As^{+3}) were detected (Fig. 7A), showing dramatic contrasts in their distributions.

In order to identify the mineral phase containing As^{+3}, detailed EDS work was performed on the same area analysed by XANES imaging (Fig. 7B). It appears that, while As^{-1} is abundant in arsenopyrite, As^{+3}

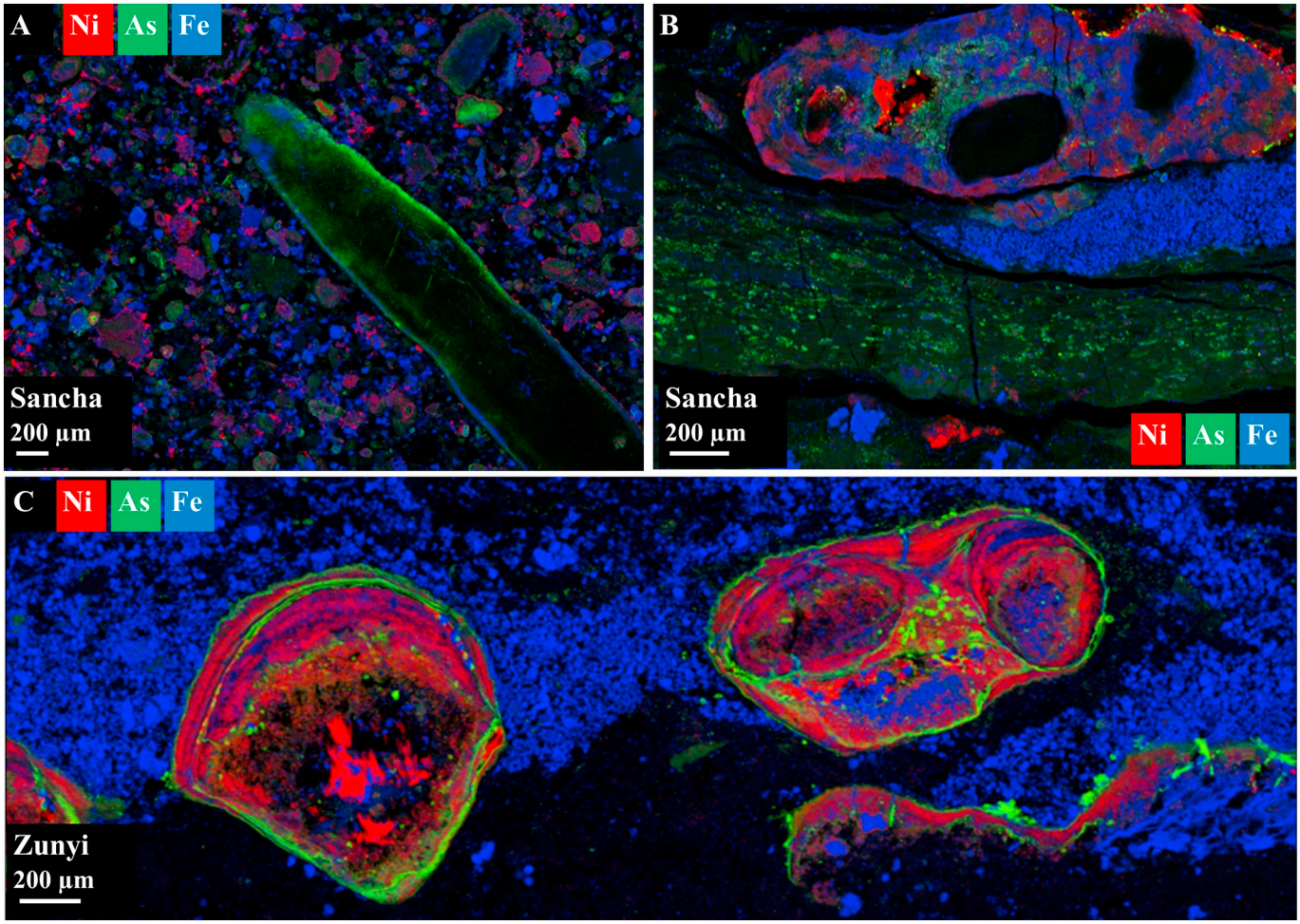

Fig. 6. Synchrotron-based XFM element maps of biogenic features showing Ni (in red), As (in green) and Fe (in blue) distributions in samples from the Sancha (A and B) and Zunyi (C) mineralised layers. (For interpretation of the references to colour in this figure legend, the reader is referred to the web version of this article.)

is mostly present in a phase that contains abundant C, Mo and S, possibly occurring as a remnant of an organic complex.

4.4. Carbon distribution

Carbon distribution in the mineralised layer from Sancha, obtained by EPMA mapping, reveals that C is highly disseminated in the mineralised layer, as highlighted in Fig. 8A. Fig. 8B shows that C is finely intergrown with pyrite, as revealed by the co-occurrence of Fe and S, but only scarcely found in phosphorite nodules.

5. Discussion

5.1. Metal and semi-metal associations

Significant enrichments in Mo, V, Cu, Ni, and Sb in sediments are commonly related to bio-accumulation, anoxic and sulfidic water column and associated sulfidation mechanisms (Brumsack, 2006). Euxinic and restricted basins, such as the Black Sea, are commonly characterised by a stratified water column and a permanent pycnocline (boundary separating two water layers of different densities) where O_2 concentrations decrease dramatically (Degens and Ross, 1974). In the part of the water column that is H_2S-rich, the solubility of Cu and Zn usually decreases significantly, and they become trapped in sulfides, commonly as sphalerite and sulvanite or covellite (Jacobs et al., 1985). In the Black Sea, Mo has been found to be trapped in the sediments, rather than in the water column (Emerson and Huested, 1991). This supports the fact that the presence of HS^- drives behavioural change of Mo from conservative to reactive, promoting its accumulation via diffusion at the water/sediment interface (Helz et al., 1996). Pyrite, in particular, has been suggested to efficiently trap As and Mo and Ni to a lesser extent (Huerta-Diaz and Morse, 1992).

However, the present results seem to mostly differ from these observations. Fig. 9 presents a summary of elemental associations observed from the Synchrotron-based XRF maps and additional SEM/EDS investigation, for samples deriving from the Sancha and Zunyi mineralised layer. Nickel is abundant but shows little association with other elements such as Fe or As. Similarly, As, although fairly abundant, does not present a strong association with Fe, suggesting that both Ni and As are not predominant in pyrite.

In a previous study on trace element affinities in the black shales of the Phosphoria Formation, USA, up to 55% of the Ni was found in association with organic matter, suggesting that Ni in black shales tends to easily form organo-metallic complexes (Perkins and Foster, 2004). Interestingly, in the Sancha mineralised layer, strong associations between Ni and the organic-rich matrix were observed, while poor associations between Ni and biogenic components were observed in the Zunyi mineralised layer (Fig. 9). Instead, at Zunyi, Ni was mainly detected with S in millerite.

Contrary to Ni, As is finely disseminated in the organic-rich matrix at both sites, showing consistent associations of As with organic matter (Fig. 9). Molybdenum in samples from Sancha, although presenting some distribution overlap with As and Fe, shows poor associations with these elements, and is also found predominantly within the organic

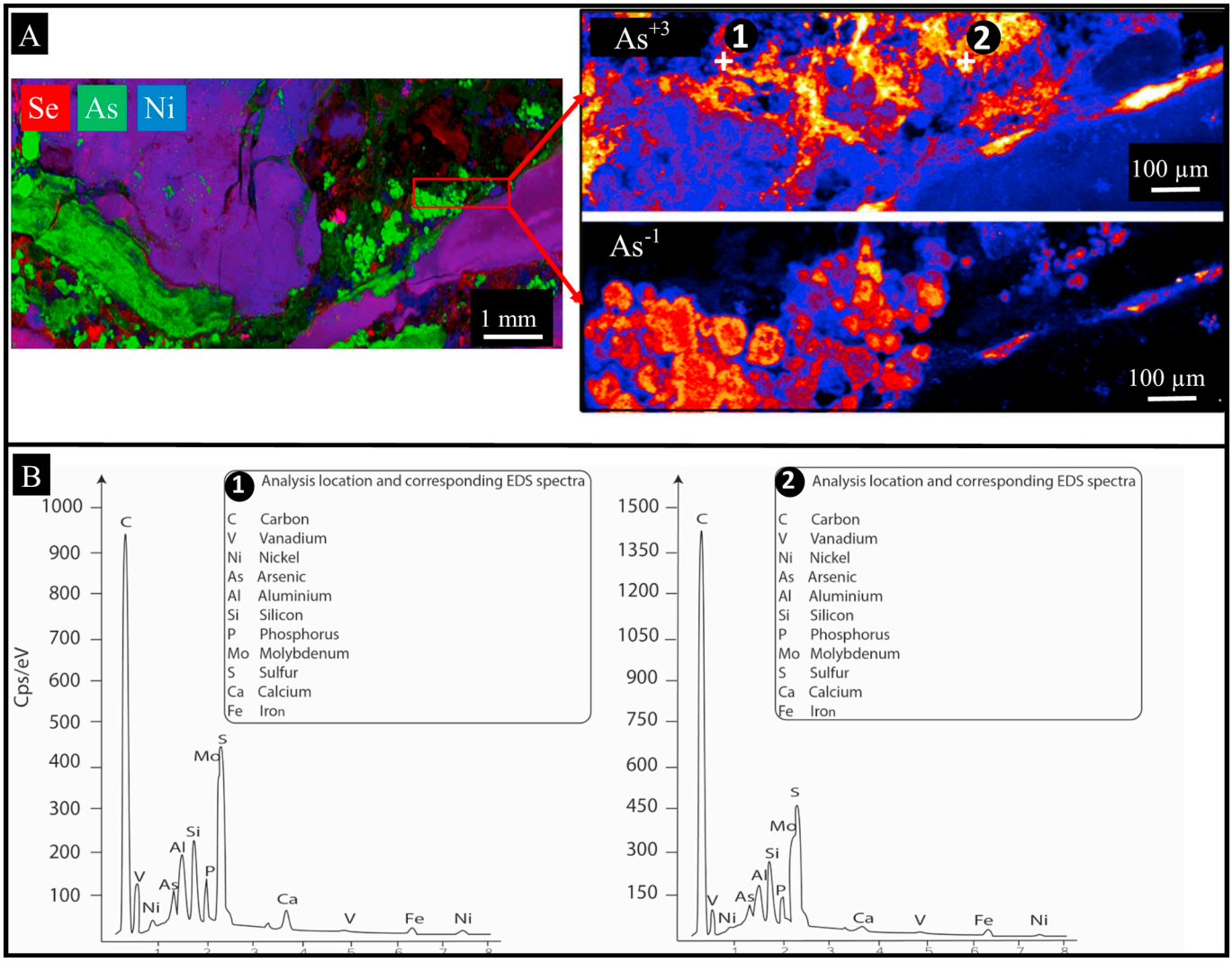

Fig. 7. A) XANES imaging for different redox states of As in a sample from the Sancha mineralised layer: As^{+3} distributions and As^{-1} distributions show contrasting textures over the same area. B) EDS spectra corresponding to point analyses 1 and 2 located on the maps.

matter-rich matrix (Fig. 9). Previous studies have reported that Mo, in the South China shales, was commonly found in a complex mineralogical mixture of Mo with S and C (Kao et al., 2001; Orberger et al., 2007), which is consistent with our observations.

Zinc and Cu distributions, however, reflect expected behaviours under euxinic conditions (Huerta-Diaz and Morse, 1992). They are much less abundant than Ni, Mo and As and show no association with Ni and As-rich phases or pyrite (Cu was only detected within pyrite in one localised area at the Sancha mineralised layer). The previous study on trace element affinities in the black shales of the Phosphoria Formation also highlighted that Zn tends to accumulate with sulfide as sphalerite and organic matter, while Cu is found with sulfide in sulvanite but also largely with organic matter (> 35% of Cu found in association with biogenic components) (Perkins and Foster, 2004). In the present study, Zn is exclusively present with S in sphalerite and Cu is found in covellite, at both sites (Fig. 9). No obvious associations with the organic-rich shaly matrix are observed, suggesting that S played the main role in accumulating Zn and Cu in these shales.

Selenium is mainly found in between pyrite aggregates and Ni and As-rich phases. While it demonstrates strong associations with Ni and As at Sancha, it only shows associations with As at Zunyi (Fig. 9). In the Phosphoria shales, Se has been suggested to be mainly present in sulfides, such as sphalerite (Zn-S), sulvanite (Cu-S), pyrite and organic matter (Perkins and Foster, 2004). In the present study, poor association of Se with Zn, Cu or Fe was found, however, Se is highly abundant in the fine organic-rich shale matrix at both sites (Fig. 9).

Overall, while organic matter appears to have promoted accumulation of metals at both sites, stronger associations of organic matter with different metals and semi-metals were visible at Sancha, even though elemental concentrations were of a similar range at both locations (e.g. 5000 ppm of Ni at Sancha and 14,000 ppm of Ni at Zunyi) (Pagès et al., 2018). Therefore, this could suggest that, despite the organic matter playing a strong role in accumulating and trapping specific metals in the sediment in the Sancha mineralised layer, it was not actually directly responsible for the extreme metal enrichment in these shales. It also supports the interpretation that local conditions within the Zunyi mineralised layer may have been slightly different, promoting a metal-S association over metal-organic matter association.

5.2. Phosphorite nodules

Abundant phosphorite nodules were detected in samples from both Zunyi and Sancha sites. As phosphorite nodules commonly lithify in the sediment and have the ability to reduce the solubility of metals, they tend to accumulate a variety of elements such as REE or Ni (e.g. Kidder et al., 2003; Seaman et al., 2001). In the present study, associations of U with these phosphorite nodules were observed for both locations. It has been shown that U can accumulate with phosphorites because U

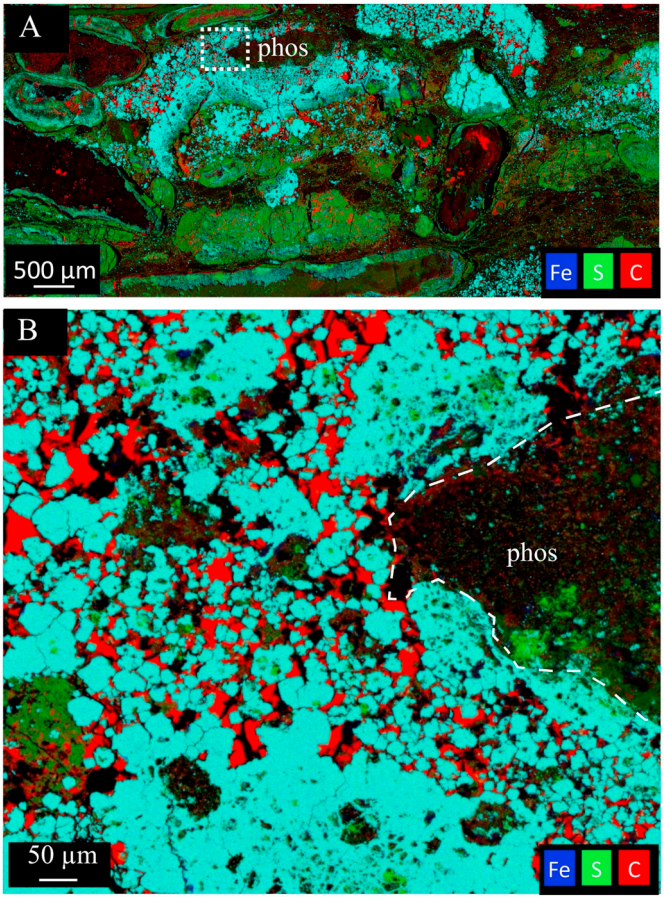

Fig. 8. Microprobe element maps of Fe (in blue), S (in green) and C (in red) distributions in a sample from the Sancha mineralised layer. The white rectangle in A) shows the area imaged in B). The dotted line in B) highlights the distribution of the phosphorite nodule in the map. (For interpretation of the references to colour in this figure legend, the reader is referred to the web version of this article.)

replaces Ca in the phosphorite (Altschuler et al., 1958), due to the radius of the tetravalent U (0.97 Å) being very similar to that of Ca (0.99 Å), and up to 90% of the U found in natural environments being tetravalent. Ni was also detected in located areas within phosphorite nodules, as highlighted in Fig. 3D. Arsenic, however, tends to be accumulating mainly on the edge of phosphorite nodules.

Phoshorite nodules can form via abiogenic and biogenic processes. The formation of these nodules can promote rapid changes in redox conditions in the surrounding environment, leading to localised accumulation in metals such as Ni and As. Phosphorite nodule formation under anoxic conditions results from the reduction of P and Fe(III) oxyhydroxides. This reactions leads to the release of Fe(II) and P into the porewater environment (Van Cappellen and Berner, 1988). In addition, P can also be accumulated in sediments via the dissolution of organic-P complexes (Filippelli, 2008), leading to P supersaturation in the sediment pore water. Murowchick et al. (1994) proposed that the phosphorite nodules of the South China metalliferous shales could have derived from microbial mats of prokaryotic organisms. Microbial mats promote localised variations in redox conditions leading to µm-scale dysaerobic microenvironments, further supporting rapid phosphate mineralisation (Pagès et al., 2015, 2014a). Extracellular polymeric substances (EPS) produced by microbial mats also trap calcium carbonate that is needed for apatite precipitation (Wilby et al., 1996). Therefore, the biogenic formation of phosphorite nodules can promote rapid changes in redox conditions in the surrounding environment, leading to localised metal accumulations such as Ni and As.

5.3. Biogenic components

The findings of the present study suggest that organic matter could have played a significant role in the accumulation of specific elements and strongly influence the µm-scale distributions of metals and semi-metals accumulated in sediments in such settings.

First, mineralised black shales from Sancha and Zunyi sites have shown to contain up to 7 wt% total organic carbon (TOC), highlighting the elevated content of organic material in the samples (Pagès et al., 2018). Second, biologically-derived features were detected in the various samples, both from the Sancha and Zunyi sites, supporting the

Sancha \ Zunyi	Ni	As	Cu	Zn	Fe	Se	Mo	Organic-rich matrix	S
Ni		Little associations in very localised areas						Little association with matrix	Abundant presence of millerite
As	Localised associations				Minor As-rich pyrite	Strong associations		As disseminated in matrix	Minor As-rich pyrite
Cu									Presence of covellite
Zn									Zn present in sphalerite
Fe	Localised Ni-rich pyrite	Localised As-rich pyrite	One localised area						Abundant pyrite
Se	Strong associations	Strong associations						Se abundant in shaly matrix	Little association in matrix
Mo					Localised Mo-rich pyrite				
Organic-rich matrix	Ni association with matrix	As disseminated in matrix				Se abundant in shaly matrix	Abundant in shaly matrix		
S	Presence of millerite	Localised As-rich pyrite	Presence of covellite	Zn present in sphalerite	Abundant pyrite	Se association in matrix	Mo association in shaly matrix	Associations in shaly matrix	

Fig. 9. Cross-tabulation of Ni, As, Cu, Zn, Fe, Se, Mo, organic-rich matrix and S showing relative associations between the different elements in samples from Sancha (green section of the table and text not underlined) and in samples from Zunyi (blue section of the table and underlined text). The green and blue cells with the absence of text highlight no visible association, the yellow colour highlights poor associations, the orange colour shows little and/or localised associations while the red colour represents strong associations. (For interpretation of the references to colour in this figure legend, the reader is referred to the web version of this article.)

evidence for shell-forming organisms. These features present strong accumulation in various metals such as Ni, As, Fe. Fine Ni-rich laminations intergrown with As and Fe-rich laminations. This is particularly interesting as a previous study conducted by Cao et al. (2013) on the mineralised layer reported the presence of organic clots, resembling that of modern red algae (Rhodophyta), displaying a preferential accumulation of Ni and Mo, with greater Mo abundance in the outer part of the cystocarp and higher Ni content in the inner part.

In addition, C distributions were heterogeneous with C finely intergrown with pyrite and seldom found in phosphorite nodules (Fig. 8). This is consistent with the previous observations from Murowchick et al. (1991) and Kříbek et al. (2007) that detected remants of carbonaceous matter, probably deriving from cyanobacterial oncolites, in phosphate grains.

5.4. Arsenic redox states reveal the influence of biogenic activity

In micro-organisms, As is involved in a wide range of metabolic functions such as assimilation, methylation, detoxification, and anaerobic respiration (Stolz et al., 2006). Arsenic has eight oxidation states from −3 to +5. As^{+1} has been previously reported in arsenopyrite from black shales (Zhu et al., 2008).

In this study, XANES experiments revealed different redox states of As (Fig. 7). As^{-1} was mainly detected in arsenopyrite. This is consistent with previous X-ray photoelectron spectroscopy study that showed that 85% of As present in arsenopyrite is present as arsenide (As^{-1}) while the remaining 15% is present as elemental As (Nesbitt et al., 1995). In addition, previous XANES measurements also highlighted that As is present as As^{-1} in arsenian pyrite (Simon et al., 1999; Savage et al., 2000; Zhu et al., 2008). In the present study, As^{+3} was also detected but did not show any association with pyrite. As^{+3} distribution actually presented a filamentous fabric possibly related to the presence of soft and flexible microbial mats.

Previous experiments conducted in black shales revealed that the mobilization of As from pyrite in incubations under sulfate reducing conditions (N_2 atmosphere, high sulfate content, high organic carbon concentration) was seven times greater than in sterile controls, suggesting that sulfide provided through bacterial sulfate-reduction drove arsenic mobilization from the solid phase (Zhu et al., 2008). This mechanism occurred via a sulfide–arsenide exchange and oxidation reaction in which sulfide replaces As in arsenopyrite to form pyrite, and arsenide (As^{-1}) is simultaneously oxidized to soluble arsenite (As^{+3}). This process was shown to be enhanced under conditions of strong redox disequilibrium, for instance in the presence of oxygen (or another oxidant such as Fe(III)) and high concentrations of sulfide (Zhu et al., 2008). Under such conditions, the following reaction can take place, mobilizing As from arsenopyrite:

$$FeAsS + HS^- + H^+ + 5/4O_2(aq) + 1/2H_2O ? FeS_2 + As(OH)_{3(aq)}$$

This reaction was shown to be strongly promoted by the activity of autotrophic arsenite-oxidizing microorganisms (Rhine et al., 2008). Rhine et al. (2008) also showed that the solubilisation of As was driven by a As(III)- and sulfur-oxidizing bacteria isolated from arsenic-containing weathered black shale. This previous study demonstrated that these organisms preferentially colonised pyrite on the surface of As-bearing black shale thick sections. Additionally, Rhine et al. (2008) emphasized that microorganisms present in the sediment can promote As mobilization and influence As speciation. Finally, this previous work also highlighted that biological activity can be directly linked to the mobilization and transformation of As from minerals under circumneutral pH.

In the present study, EDS analysis supports that the As^{+3} detected by XANES imaging is mostly associated with the complex MoSC mixture. This is of particular interest as As and Mo distributions have been previously suggested to be influenced by biogenic components (Cao et al., 2013) and because the complex mineralogical mixture of Mo with S and C identified in the South China shales (Orberger et al., 2007) has not been reported elsewhere in the world. In addition, at the nanoscale, MoSC displays nanometric porous rounded structures of molybdenite finely intergrown with organic matter and circular structures showing striking similarity with bacterial cells (Kao et al., 2001). The characterisation of the MoSC phase appears of significant importance as previous studies have shown that adenine ($C_5H_5N_5$), a biomolecule playing a significant role in metabolic and genetic processes strongly adsorbs on surfaces of MoS_2 and could have been a significant factor in the emergence of life (Sowerby et al., 1998; Hazen, 2005). Therefore, organic matter associations with Mo and As can provide further insight into the biological processes related to the Cambrian radiation (Steiner et al., 2001; Mao et al., 2002).

In this study, the detection of As^{-1} in arsenopyrite and adjacent As^{+3} in the MoSC phase regarded as a complex mixture of C and MoS_2 (Kao et al., 2001) therefore suggests that microbial activity strongly contributed to the occurrence of redox disequilibrium in the sediment, through the production of sulfide by sulfate-reducing bacteria and the possible production of oxidants via additional microbial activities. In addition, it is possible that the preferential accumulation of As^{+3} in the MoSC was related to the role of organic matter in trapping As. These results are strongly in favour of a biogenic involvement in the distributions of As and Mo, and potentially at a larger scale, in the ore formation itself.

5.5. Redox conditions and microbial activity

Synchrotron XFM mapping highlighted strong heterogeneities in μm-scale metal distributions within samples from both the Zunyi and the Sancha mineralised layers, likely reflecting rapid changes in redox conditions in the sediments. Evidence from this study, combined with previous studies, highlight the importance of a biogenic component in the genetic processes at play. The XANES imaging of As redox states, in particular, reemphasized μm-scale variations in redox conditions and the likely role of microbial communities in promoting redox disequilibrium in the sediment, therefore promoting metal enrichment.

Previous studies have supported the interpretation that the South China metalliferous shales were deposited under euxinic (anoxic and sulfidic) conditions (e.g., Pi et al., 2013). Under such conditions, sulfide accumulates as a result of bacterial sulfate reduction. Sulfate reduction is a key respiratory pathway (anaerobic respiration) (Canfield and Des Marais, 1993) that uses sulfate as the terminal electron acceptor, leading to the production of H_2S. Scott et al. (2017) recently proposed that intense H_2S accumulations associated with phototrophic sulfide-oxidizing bacterial activity in the water column would promote high TOC values and metal concentrations in the mineralised shales of the Bakken Formation, USA. In such environments, redox conditions can play a crucial role on metal accumulation and distribution.

Modern microbial mats containing sulfur-cycling microorganisms have been observed to thrive under such euxinic conditions. The main factors controlling distribution of sulfur-oxidizing microbial mats remain poorly understood, although H_2S content, O_2 and nitrate concentrations of the overlying water, as well as bacterial sulfate-reduction in the underlying sediment have been suggested to play a role in the distribution and metabolic rates of sulfur-oxidizing microbial mats (Joye et al., 2004; Joye et al., 2009). Such mats of sulfide-oxidizing bacteria have been commonly reported in oxygen minimum zones of sediments, for instance along the Costa Rica Margin in the Gulf of Mexico, where H_2S is being produced by anaerobic respiration (Bailey et al., 2009). In addition, under such conditions, neutrophilic Fe(II)-oxidizing bacteria have been recognised to also form mats and promote mineral precipitation (Emerson and Moyer, 2002).

In modern microbial mats, microbial communities have been shown to promote very strong redox disequilibrium leading to the presence of μm-scale microenvironments (Pagès et al., 2014a; Pagès et al., 2015). Two-dimensional mapping of microbial sulfate reduction in Bahamas

microbial mats have shown strong lateral and vertical heterogeneity in the activity of sulfate-reducing bacteria (SRB) resulting in highly variable sulfide distribution in the mat (Visscher et al., 2000; Dupraz et al., 2004). In addition, in modern microbial mats, variations in O_2 concentrations have been observed on a scale of microns, leading to highly dynamic μm-scale variations between oxygen supersaturation and anoxic conditions (Paerl and Pinckney, 1996). Two-dimensional mapping of sulfide, alkalinity, iron(II) and phosphate concentrations in modern Shark Bay mats also revealed μm-scale variations in distributions within the mats and associated sediments (Pagès et al., 2014b). Furthermore, highly heterogeneous distributions of Zn, Mn and As were also reported in modern microbial mats (Davison et al., 1997). Such variations in concentrations could be associated with changes in the surface topography of the microbial mats, affecting the properties of the diffusive boundary layer and therefore promoting lateral heterogeneity in porewater analytes distributions (Jørgensen, 1994).

Previous studies on the South China mineralised layer reported that abundant sponge spicules and remnants of bivalve arthropods were present at both Zunyi and Sancha sites, with localised areas containing hundreds of disarticulated valves of bivalves (Steiner al., 2001). It was proposed that fluctuations of redox conditions would have led arthropods to colonise specific areas and feed on the chemolithotrophic microbial mats. In addition, structures presenting strong similarities with phototrophic coccoid cyanobacteria throughout the mineralised samples have been observed (Kříbek et al., 2007). These findings suggested that the deposition of the mineralised layer most likely occurred at the limit of light penetration where bacteria could perform anoxygenic photosynthesis.

Consequently, the combination of previous and present observations suggests that the significant μm-scale variations in metal distributions observed in the mineralised layer at Sancha and Zunyi, along with the formation of phosphorite nodules, could have been strongly promoted by dynamic microbial activity in the sediments.

6. Conclusion

Our study presents a detailed μm-scale investigation of metal and semi-metal distributions and associations in the sulfide polymetallic layer at two locations, Zunyi and Sancha, located hundreds of km apart in South China. Strong μm-scale variations in metal and semi-metal distributions were highlighted by Synchrotron-based XRF mapping at both sites. At both sites, U is predominantly found within phosphorite nodules while As, Mo and Se are particularly abundant in the organic-rich matrix, showing strong associations with organic matter. Nickel, however, shows different distributions between the two sites. It is predominantly found with the organic matter at the Sancha site while it is mainly detected in millerite at the Zunyi site, suggesting that the local conditions at Zunyi may have promoted Ni-S associations over Ni-organic matter. Also at both sites, biogenic features were re-mineralised with laminations dominated by different metals, indicating a possible control of organic matter over metal distributions. In addition, the XANES imaging highlighted different redox states of As over μm-scale area. While As^{-1} appears to be mainly present in pyrite, As^{+3} was mainly detected in association with an organic MoSC phase. This remobilisation of As and change in its redox state was likely driven by microbial activity in the sediment, as previously described in other black shales under experimental conditions.

Overall, the present results emphasize the complexity of metal distributions in this mineralised layer, the crucial role of organic matter in the accumulation and precipitation of semi-metals and metals in these metal-rich black shales and highlight how biogenic activity can promote μm-scale variations in redox conditions in sedimentary environments.

Acknowledgments

The synchrotron X-ray fluorescence maps were undertaken on the X-ray Fluorescence Microscopy beamline at the Australian Synchrotron, part of ANSTO, and we acknowledge the assistance of Daryl Howard and Martin De Jonge. We acknowledge financial support for this facility from the Science and Industry Endowment Fund (SIEF). We also acknowledge financial support from the strategic Priority Research Program (B) of Chinese Academy of Sciences (Grant No. XDB18000000) and Open fund of SKLODG (State Key Lab of Ore Deposit Geochemistry).

The PIXE maps were collected on the CSIRO-MARC Nuclear Microprobe hosted on the University of Melbourne Pelletron accelerator. We acknowledge the assistance of Roland Szymanski and Stephen Gregory in the operation of the Pelletron.

References

Altschuler, Z.S., Cigar, R.S., Young, E.Y., 1958. Geochemistry of uranium in apatite and phosphorite. US Geol. Surv. Prof. Pap. 314, 45–90.
Bailey, J.V., Orphan, V.J., Joye, S.B., Corsetti, F.A., 2009. Chemotrophic microbial mats and their potential for preservation in the rock record. Astrobiology 9, 843–859.
Brumsack, H.-J., 2006. The trace metal content of recent organic carbon-rich sediments: implications for Cretaceous black shale formation. Palaeogeogr. Palaeoclimatol. Palaeoecol. 232, 344–361.
Canfield, D.E., Des Marais, D.J., 1993. Biogeochemical cycles of carbon, sulfur, and free oxygen in a microbial mat. Geochim. Cosmochim. Acta 57, 3971–3984.
Cao, J., Hu, K., Zhou, J., Shi, C., Bian, L., Yao, S., 2013. Organic clots and their differential accumulation of Ni and Mo within early Cambrian black-shale-hosted polymetallic Ni-Mo deposits, Zunyi, South China. J. Asian Earth Sci. 62, 531–536 (A).
Condon, D., Zhu, M.-Y., Bowring, S., Wang, W., Yang, A.-H., Jin, Y.-G., 2005. U–Pb ages from the Neoproterozoic Doushantuo Formation, China. Science 308, 95–98.
Coveney Jr., R.M., Chen, N.S., 1991. Ni-Mo-PGE-Au-rich ores in Chinese black shales and speculations on possible analogues in the United States. Mineral. Deposita 26, 83–88.
Coveney, R.M., Nansheng, C., 1991. Ni-Mo-PGE-Au-rich ores in Chinese black shales and speculations on possible analogues in the United States. Miner. Depos. 26, 83–88.
Davison, W., Fones, G.R., Grime, G.W., 1997. Dissolved metals in surface sediment and a microbial mat at 100-|[mu]|m resolution. Nature 387, 885–888.
Degens, E.T., Ross, D.A., 1974. The Black Sea - geology, chemistry, and biology. In: Am. Assoc. Pet. Geol. vol. 20. AAPG Mem. Tulsa, Oklahoma, pp. 633.
Dupraz, C., Visscher, P.T., Baumgartner, L.K., Reid, R.P., 2004. Microbe-mineral interactions: early carbonate precipitation in a hypersaline lake (Eleuthera Island, Bahamas). Sedimentology 51, 745–765.
Emerson, S.R., Huested, S.S., 1991. Ocean anoxia and the concen- trations of molybdenum and vanadium in seawater. Mar. Chem. 34, 177–196.
Emerson, D., Moyer, C.L., 2002. Neutrophilic Fe-oxidizing bacteria are abundant at the Loihi seamount hydrothermal vents and play a major role in Fe oxide deposition. Appl. Environ. Microbiol. 68, 3085–3093.
Emsbo, P., Hofstra, A.H., Johnson, C.A., Koenig, A., Grauch, R., Zhang, X., Hu, R., Su, W., Pi, D., 2005. Lower cambrian metallogenesis of south China: interplay between diverse basinal hydrothermal fluids and marine chemistry. In: Mineral Deposit Research: Meeting the Global Challenge. Springer Berlin Heidelberg, pp. 115–118.
Etschmann, B.E., Donner, E., Brugger, J., Howard, D.L., de Jonge, M.D., Paterson, D., Naidu, R., Scheckel, K.G., Ryan, C.G., Lombi, E., 2014. Speciation mapping of environmental samples using XANES imaging. Environ. Chem. 11, 341–350.
Fan, D., 1983. In: Augstithis, S.S. (Ed.), Fan, D., 1983. Polyelements in the Lower Cambrian black shale series in southern China. In Augstithis, S.S., ed. The significance of trace metals in solving petrogenetic problems and controversies: Athens, Greece, Theophrastus Publications, p. 447-474. Theophrastus Publications, Athens, Greece, pp. 447–474.
Filippelli, G.M., 2008. The global phosphorus cycle: past, present and future. Elements 4, 89–95.
Gradstein, F., Ogg, J., Smith, A. (Eds.), 2004. A Geologic Time Scale 2004. Cambridge University Press, Cambridge (589 pp.).
Harrowfield, I.R., MacRae, C.M., Wilson, N.C., 1993. Chemical imaging in electron microprobes. In: Proc. 27th Annu. MAS Meet. (Microbema Anal. Soc.), pp. 547–548.
Hazen, R.M., 2005. Genesis: rocks, minerals and geochemical origin of life. Elements 1, 135–137.
Helz, G.R., Miller, C.V., Charnock, J.M., Mosselmans, J.F.W., Pattrick, R. a D., Garner, C.D., Vaughan, D.J., 1996. Mechanism of molybdenum removal from the sea and its concentration in black shales: EXAFS evidence. Geochim. Cosmochim. Acta 60, 3631–3642.
Huerta-Diaz, M.A., Morse, J.W., 1992. Pyritization of trace metals in anoxic marine sediments. Geochim. Cosmochim. Acta 56, 2681–2702.
Jacobs, L., Emerson, S., Skei, J., 1985. Partitioning and transport of metals across the O2/H2S interface in a permanently anoxic basin: Framvaren Fjord, Norway. Geochim. Cosmochim. Acta 49, 1433–1444.
Jiang, S.-Y., Chen, Y.-Q., Ling, H.-F., Yang, J.-H., Feng, H.-Z., Ni, P., 2006. Trace- and rare-earth element geochemistry and Pb-Pb dating of black shales and intercalated Ni-Mo-PGE-Au sulfide ores in Lower Cambrian strata, Yangtze Platform, South China.

Miner. Depos. 41, 453–467.
Jørgensen, B.B., 1994. Sulfate reduction and thiosulfate transformations in a cyanobacterial mat during a diel oxygen cycle. FEMS Microbiol. Ecol. 13, 303–312.
Joye, S.B., Boetius, A., Orcutt, B.N., Montoya, J.P., Schulz, H.N., Erickson, M.J., Lugo, S.K., 2004. The anaerobic oxidation of methane and sulfate reduction in sediments from Gulf of Mexico cold seeps. Chem. Geol. 205, 219–228.
Joye, S.B., Samarkin, V.A., Orcutt, B.N., MacDonald, I.R., Hinrichs, K.-U., Elvert, M., Teske, A.P., Lloyd, K.G., Lever, M.A., Montoya, J.P., Meile, C.D., 2009. Metabolic variability in seafloor brines revealed by carbon and sulphur dynamics. Nat. Geosci. 2, 349–354.
Kao, L.S., Peacor, D.R., Coveney, J., Zhao, G., Dungey, K.E., Curtis, M.D., Penner-Hahn, J.E., 2001. A C/MoS2 mixed-layer phase (MoSC) occurring in metalliferous black shales from Southern China, and new data on jordisite. Am. Mineral. 86, 852–861.
Kidder, D.L., Krishnaswamy, R., Mapes, R.H., 2003. Elemental mobility in phosphatic shales during concretion growth and implications for provenance analysis. Chem. Geol. 198, 335–353.
Kříbek, B., Sýkorová, I., Pašava, J., Machovič, V., 2007. Organic geochemistry and petrology of barren and Mo–Ni–PGE mineralized marine black shales of the Lower Cambrian Niutitang Formation (South China). Int. J. Coal Geol. 72, 240–256.
Laird, J.S., Ryan, C.G., Kirkham, R., Satoh, T., Pages, A., 2017. Next generation data acquisition systems for the CSIRO Nuclear Microprobe: Highly scaled versus customizable. Nucl. Instruments Methods Phys. Res. Sect. B Beam Interact. with Mater. Atoms 404, 15–20.
Lehmann, B., Frei, R., Xu, L., Mao, J., 2016. Early cambrian black shale-hosted Mo-Ni and V mineralization on the rifted margin of the Yangtze platform, China: Reconnaissance chromium isotope data and a refined metallogenic model. Econ. Geol. 111, 89–103.
Lehmann, B., Nägler, T.F., Holland, H.D., Wille, M., Mao, J., Pan, J., Dulski, P., 2007. Highly metalliferous carbonaceous shale and early Cambrian seawater. Geology 35, 403–406.
Li, S., Gao, Z., 2000. Source tracing of noble metal elements in Lower Cambrian black rock series of Guizhou-Hunan Provinces, China. Sci. China Ser. D Earth Sci. 43, 625–632.
Lott, D.A., Coveney, R.M., Murowchick, J.B., Grauch, R.I., 1999. Sedimentary exhalative nickel-molybdenum ores in South China. Econ. Geol. 94, 1051–1066.
Mao, J., Lehmann, B., Du, A., Zhang, G., Ma, D., Wang, Y., Zeng, M., Kerrich, R., 2002. Re-Os dating of polymetallic Ni-Mo-PGE-Au mineralization in Lower Cambrian black shales of South China and its geologic significance. Econ. Geol. 97, 1051–1061.
Murowchick, J.B., Coveney Jr., R.M., Grauch, R.I., Shelton, K.L., 1991. Mo-Ni-bearing cyanobacterial oncolites from the Cambrian of China. GSA Annual Mtg. Abstr. Prog. 23, A172.
Murowchick, J.B., Coveney, R.M., Grauch, R.I., Eldridge, C.S., Shelton, K.L., 1994. Cyclic variations of sulfur isotopes in Cambrian stratabound Ni-Mo-(PGE-Au) ores of southern China. Geochim. Cosmochim. Acta 58, 1813–1823 (A).
Nesbitt, W.H., Muir, J., Praw, A.R., 1995. Oxidation of arsenopyrite by air and air-saturated, distilled water, and implications for mechanism of oxidation. Geochim. Cosmochim. Acta 59, 1773–1786.
Orberger, B., Vymazalova, a., Wagner, C., Fialin, M., Gallien, J.P., Wirth, R., Pasava, J., Montagnac, G., 2007. Biogenic origin of intergrown Mo-sulphide- and carbonaceous matter in Lower Cambrian black shales (Zunyi Formation, southern China). Chem. Geol. 238, 213–231.
Paerl, H.W., Pinckney, J.L., 1996. A mini-review of microbial consortia: their roles in aquatic production and biogeochemical cycling. Microb. Ecol. 31, 225–247. Available at. http://link.springer.com/10.1007/BF00171569, Accessed date: 19 July 2018.
Pagès, A., Grice, K., Vacher, M., Welsh, D.T., Teasdale, P.R., Bennett, W.W., Greenwood, P., 2014a. Characterizing microbial communities and processes in a modern stromatolite (Shark Bay) using lipid biomarkers and two-dimensional distributions of porewater solutes. Environ. Microbiol. 16, 2458–2474.
Pagès, A., Welsh, D.T., Teasdale, P.R., Grice, K., Vacher, M., Bennett, W.W., Visscher, P.T., 2014b. Diel fluctuations in solute distributions and biogeochemical cycling in a hypersaline microbial mat from Shark Bay, WA. Mar. Chem. 167, 102–112.
Pagès, A., Grice, K., Welsh, D.T., Teasdale, P.T., Van Kranendonk, M.J., Greenwood, P., 2015. Lipid biomarker and isotopic study of community distribution and biomarker preservation in a laminated microbial mat from Shark Bay, Western Australia. Microb. Ecol. 70, 459–472.
Pagès, A., Barnes, S., Schmid, S., Coveney Jr., R.M., Schwark, L., Liu, W., Grice, K., Fan, H., Wen, H., 2018. Geochemical investigation of the lower Cambrian mineralised black shales of South China and the late Devonian Nick deposit, Canada. Ore Geol. Rev. 94, 396–413.
Pašava, J., Kříbek, B., Vymazalová, A., Sýkorová, I., Žák, K., Orberger, B., 2008. Multiple sources of metals of mineralization in Lower Cambrian black shales of South China: evidence from geochemical and petrographic study. Resour. Geol. 58, 25–42.
Perkins, R.B., Foster, A.L., 2004. Chapter 10 Mineral affinities and distribution of selenium and other trace elements in black shale and phosphorite of the phosphoria formation. Handb. Explor. Environ. Geochemistry 8, 251–295.
Pi, D., Liu, C., Shields-zhou, G.A., Jiang, S., 2013. Trace and rare earth element geochemistry of black shale and kerogen in the early Cambrian Niutitang Formation in Guizhou province, South China: Constraints for redox environments and origin of metal enrichments. Precambrian Res. 225, 218–229.
Rhine, E.D., Onesios, K.M., Serfes, M.E., Reinfelder, J.R., Young, L.Y., 2008. Arsenic transformation and mobilization from minerals by the arsenite oxidizing strain WAO. Environ. Sci. Technol. 42, 1423–1429.
Ryan, C., 2004. Ion beam microanalysis in geoscience research. Nucl. Instruments Methods Phys. Res. Sect. B Beam Interact. with Mater. Atoms 219–220, 534–549.
Ryan, C.G., Jamieson, D.N., 1993. Dynamic analysis: on-line quantitative PIXE microanalysis and its use in overlap-resolved elemental mapping. Nucl. Instruments Methods Phys. Res. Sect. B Beam Interact. with Mater. Atoms 77, 203–214.
Ryan, C.G., Siddons, D.P., Kirkham, R., Dunn, P.A., Kuczewski, A., Moorhead, G., De Geronimo, G., Paterson, D.J., de Jonge, M.D., Hough, R.M., Lintern, M.J., Howard, D.L., Kappen, P., Cleverley, J., Denecke, M., Walker, C.T., 2010. The new Maia detector system: methods for high definition trace element imaging of natural material. AIP Conference Proceedings 9–17.
Savage, K.S., Tingle, T.N., O'Day, P.A., Waychunas, G.A., Bird, D.K., 2000. Arsenic speciation in pyrite and secondary weathering phases, Mother Lode Gold District, Tuolumne County, California. Appl. Geochem. 15, 1219–1244.
Scott, C.T., Slack, J.F., Kelley, K.D., 2017. The hyper-enrichment of V and Zn in black shales of the late Devonian-early Mississippian Bakken Formation (USA). Chem. Geol. 452, 24–33.
Seaman, J.C., Arey, J.S., Bertsch, P.M., 2001. Immobilization of Ni and other metals in contaminated sediments using soil amendments. J. Environ. Qual 30, 460–469.
Simon, G., Huang, H., Penner-Hahn, J.E., Kesler, S.S.E., Kao, L.-S., 1999. Oxidation state of gold and arsenic in gold-bearing arsenian pyrite. Am. Miner. 84, 1071–1079.
Sowerby, S.J., Edelwirth, M., Heckl, W.M., 1998. Self-assembly at the prebiotic solid – liquid interface: structures of self-assembled monolayers of adenine and guanine bases formed on inorganic surfaces. J. Phys. Chem. 102, 5914–5922. Available at. https://pubs.acs.org/doi/abs/10.1021/jp980684l, Accessed date: 19 July 2018.
Steiner, M., Wallis, E., Erdtmann, B.D., Zhao, Y., Yang, R., 2001. Submarine-hydrothermal exhalative ore layers in black shales from South China and associated fossils - insights into a Lower Cambrian facies and bio-evolution. Palaeogeogr. Palaeoclimatol. Palaeoecol. 169, 165–191.
Stolz, J.F., Basu, P., Santini, J.M., Oremland, R.S., 2006. Arsenic and selenium metabolism. Annu. Rev. Microbiol. 60, 107–130.
Van Cappellen, P., Berner, R., 1988. A mathematical model for the early diagenesis of phosphorus and fluorine in marine sediments. Apatite precipitation. Am. J. Sci. 288, 289–333.
Visscher, P.T., Pamela Reid, R., Bebout, B.M., 2000. Microscale observations of sulfate reduction: correlation of microbial activity with lithified micritic laminae in modern marine stromatolites. Geology 28, 919.
Wallis, E., 2007. The climatic and environmental history of the South Chinese Yangtze platform during the Neoproterozoic and Early Cambrian: hydrothermally active and salinity stratified epicontinental basins a key for understanding the "Cambrian explosion"? Ph.D Thesis. Berlin. pp. 227 (in German with English abstract).
Wilby, P.R., Briggs, D.E.G., Bernier, P., Gaillard, C., 1996. Role of microbial mats in the fossilization of soft tissues. Geology 24, 787.
Xu, L., Lehmann, B., Mao, J., 2013. Seawater contribution to polymetallic Ni–Mo–PGE–Au mineralization in Early Cambrian black shales of South China: evidence from Mo isotope, PGE, trace element, and REE geochemistry. Ore Geol. Rev. 52, 66–84.
Zeng, M., 1998. Geological characteristics of the Huangjiawan Mo-Ni deposit and its development in the future. Guizhou Geol 15, 305–310.
Zhu M.-Y., Zhang J.-M., Steiner M., Yang A., Li G.-X. and Erdtmann B.-D. (2003) Sinian–Cambrian stratigraphic framework for shallow to deep-water environments of the Yangtze Platform: an integrated approach. Prog. Nat. Sci. 13, 946–950.
Zhu, W., Young, L.Y., Yee, N., Serfes, M., Rhine, E.D., Reinfelder, J.R., 2008. Sulfide-driven arsenic mobilization from arsenopyrite and black shale pyrite. Geochim. Cosmochim. Acta 72, 5243–5250.